Angular momentum projection of cranked Hartree-Fock states: Application to terminating bands in $A \sim 44$ nuclei

H. Zduńczuk,[1] W. Satuła,[1] J. Dobaczewski,[1,2] and M. Kosmulski[3]

[1]*Institute of Theoretical Physics, University of Warsaw, ul. Hoża 69, PL-00-681 Warsaw, Poland*
[2]*Department of Physics, Post Office Box 35 (YFL), FI-40014 University of Jyväskylä, Finland*
[3]*Department of Physics, University of Warsaw, ul. Hoża 69, PL-00-681 Warsaw, Poland*

We present the first systematic calculations based on the angular momentum projection of cranked Slater determinants. We propose the $I_y \rightarrow I$ scheme, by which one projects the angular momentum I from the one-dimensional cranked state constrained to the average spin projection of $\langle \hat{I}_y \rangle = I$. Calculations performed for the rotational band in ^{46}Ti show that the AMP $I_y \rightarrow I$ scheme offers a natural mechanism for correcting the cranking moment of inertia at low spins and shifting the terminating state up by ~ 2 MeV, in accordance with data. We also apply this scheme to high-spin states near the band termination in $A \sim 44$ nuclei and compare results thereof with experimental data, shell-model calculations, and results of the approximate analytical symmetry-restoration method proposed previously.

I. INTRODUCTION

The energy density functional (EDF) method in nuclear physics is nowadays the approach of choice for large-scale nuclear structure calculations. It has the same roots as the density functional theory (DFT) [1] in atomic and molecular physics, which is based on the Coulomb interaction between electrons. In nuclear physics, the EDF approach still lacks firm microscopic derivation and well-defined rules that would allow for systematic construction of an exact (or optimal) functional. In practice, the nuclear EDF is constructed phenomenologically, based on the knowledge accumulated within modern self-consistent mean-field approaches built upon an effective density-dependent two-body interaction.

These approaches, although successful in reproducing gross nuclear properties and certain generic features of collective and single-particle nuclear motion, are only coarse in confrontation with precise spectroscopic data. This situation calls for improvement, which can be achieved in two directions, namely, either *explicitly*, by using better and/or richer parametrizations of the nuclear EDF, or *implicitly*, by going beyond the mean-field or Hartee-Fock (HF) level. At present, intense studies are being conducted in both directions, aiming at exploring the limits thereof and answering the question of whether these two directions can be considered equivalent, complementary, or independent of one another. In this work we will explore the second alternative, by employing the angular-momentum-projection (AMP) method of cranked HF (CHF) states.

A few words clarifying the terminology used in this paper are in order. In principle, the EDF methods are supposed to describe the exact ground states of many-fermion systems, including many types of different correlations. This is exactly the aim of our study, namely, to describe rotational properties of correlated states forming rotational bands. The EDF approach is not based on any HF approximation; however, it leads to the mean-field equations, which have a form analogous to that of the HF method. Therefore, the name HF is widely used in nuclear physics, and in the present study we also follow this well-accepted tradition. Nevertheless, the methods used here rely in their spirit on the EDF approach, and the Skyrme effective interactions are only providing suitable parametrizations of the underlying density functionals. Clearly, the energies of the AMP states are still functionals of the unprojected one-body densities.

The spontaneous symmetry breaking (SSB) mechanism is inherently built into the HF approach. In many cases, it not only allows for incorporating a significant fraction of many-body correlations into a single HF state, but it also serves as a source of deep physical intuition. Emergence of nuclear deformation (breaking of rotational invariance) leads naturally to the collective rotational motion and is one of the most spectacular manifestations of SSB in nuclear physics.

The CHF approximation treats collective (rotational) and intrinsic degrees of freedom on the same self-consistent footing. This fact is at the base of the success of this simple approximation, because in atomic nuclei both energy scales are strongly interwoven, and dramatic structural changes may take place along rotational bands. Terminating rotational bands [2] are the best examples of such possible changes, whereupon the collective rotation is followed by the total alignment of valence particles.

Although the energies of rotational states are correctly reproduced by the CHF approach, and the changes of shape and pairing as well as the recoupling processes of individual nucleonic orbits are well captured, the price paid is high. Indeed, the resulting wave packets (deformed CHF states) $|\Phi_{I_y}\rangle$ are well localized in the angular degrees of freedom and thus they are broadly spread over many angular momenta $|\Phi_{I_y}\rangle = \sum_I w_I |I\rangle$, with only the average value of the projection of angular momentum on one of the axes (the y axis in our case) being constrained:

$$\langle \Phi_{I_y} | \hat{I}_y | \Phi_{I_y} \rangle \equiv \langle \hat{I}_y \rangle = I_y. \tag{1}$$

Apart from strongly deformed states, this feature of the cranking approximation precludes applications of this formalism to compute transition rates, which constitute an extremely

valuable source of structural information. The demand for symmetry restoration is therefore well motivated. Starting from the deformed CHF state $|\Phi_{I_y}\rangle$, the goal can be achieved by projecting onto the eigenspaces of the angular momentum. Most of the calculations that have been performed so far invoke the angular momentum method applied to nonrotating states (see, e.g., Refs. [3–5] and the reviews in Refs. [6–9]). This limits their applicability to low spin states, where the influence of rotation on the intrinsic states can be neglected, and leads to an overestimate of the nuclear moment of inertia (MoI) as compared to the (realistic) cranking estimate.

After the ground-breaking studies performed within the phenomenological [10,11] and self-consistent [12,13] mean-field frameworks, the AMP of cranked states has not been performed in modern calculations. Recently, in Ref. [14], we presented results of such calculations for the test case of collective rotation of a well-deformed nucleus ^{156}Gd. The AMP procedure we used has been implemented within the code HFODD [15,16]. The calculational scheme proposed and tested in Ref. [14], dubbed hereafter the $I_y \to I$ scheme, assumes the AMP of spin component I of the self-consistent CHF state $|\Phi_{I_y}\rangle$, which is constrained to the same mean value of the projection on the y axis (i.e., $\langle \hat{I}_y \rangle = I$). It combines the simplicity of the self-consistent one-dimensional cranking approach, and its ability to reproduce the correct MoI, with the AMP after variation method.

In this paper, within the same formalism, we present the first systematic calculations of rotational states along terminating bands in the $A \sim 44$ mass region. The paper is organized as follows. Methods of calculation and results are presented in Secs. II and III, respectively. In particular, the AMP of cranked states along the rotational band in ^{46}Ti is discussed in Sec. III A and the AMP of states near the band termination is presented in Sec. III B. Finally, a summary and discussion are given in Sec. IV.

II. METHODS

The angular-momentum-conserving wave function is obtained by employing the standard operator $\hat{P}^I_{MK}$ [17,18] projecting onto angular momentum I, with projections M and K along the laboratory and intrinsic z axes, respectively,

$$|IMK\rangle = \hat{P}^I_{MK}\left|\Phi_{I_y}\right\rangle \equiv \frac{2I+1}{8\pi^2} \int D^{I*}_{MK}(\Omega)\hat{R}(\Omega)|\Phi_{I_y}\rangle d\Omega. \tag{2}$$

Here, Ω represents the set of three Euler angles $\alpha\beta\gamma$, $D^{I*}_{MK}(\Omega)$ are the Wigner functions [19], and $\hat{R}(\Omega) = e^{-i\alpha\hat{I}_z}e^{-i\beta\hat{I}_y}e^{-i\gamma\hat{I}_z}$ is the rotation operator.

Since K is not a good quantum number, different K components must be mixed with the mixing coefficients determined by the minimization of energy. The K-mixing is realized in a standard way by assuming

$$|IM\rangle^{(i)} = \sum_K g^{(i)}_K |IMK\rangle \equiv \sum_K g^{(i)}_K \hat{P}^I_{MK}|\Phi\rangle \tag{3}$$

and by solving the following Hill-Wheeler (HW) [20] equation:

$$\mathcal{H}\bar{g}^{(i)} = E_i \mathcal{N}\bar{g}^{(i)}, \tag{4}$$

where $\mathcal{H}_{K'K} = \langle\Phi|\hat{H}\hat{P}^I_{K'K}|\Phi\rangle$ and $\mathcal{N}_{K'K} = \langle\Phi|\hat{P}^I_{K'K}|\Phi\rangle$ denote the Hamiltonian and overlap kernels, respectively, and $\bar{g}^{(i)}$ denotes a column of the $g^{(i)}_K$ coefficients. The overlap and Hamiltonian kernels have their standard functional form but depend upon transition (or mixed) density matrices between rotated states:

$$\rho_{\alpha\beta}(\Omega) = \frac{\langle\Phi|a^+_\beta a_\alpha \hat{R}(\Omega)|\Phi\rangle}{\langle\Phi|\hat{R}(\Omega)|\Phi\rangle}. \tag{5}$$

The transition density matrix is also used for the density-dependent term. This is the only prescription available so far satisfying certain consistency criteria, formulated and thoroughly discussed in Refs. [5,21].

Owing to the overcompleteness of the $|IMK\rangle$ states, Eq. (4) is solved within the so-called collective subspace spanned by the natural states,

$$|mIM\rangle = \frac{1}{\sqrt{n_m}} \sum_K \eta^{(m)}_K |IMK\rangle, \tag{6}$$

which are eigenstates of the norm matrix $\mathcal{N}_{K'K}$ having nonzero eigenvalues ($n_m \neq 0$):

$$\mathcal{N}\bar{\eta}^{(m)} = n_m \bar{\eta}^{(m)}. \tag{7}$$

In practical applications, the cutoff parameter ζ is used and the collective subspace is constructed by using only those natural states that satisfy $n_m \geq \zeta$. By ordering indices m of the natural states in such a way that larger indices correspond to smaller norm eigenvalues, we can write the solutions of the HW equation (4) as

$$|IM\rangle^{(i)} = \sum_{m=1}^{m_{\max}} f^{(i)}_m |mIM\rangle, \tag{8}$$

where the mixing coefficients of Eq. (3) read

$$g^{(i)}_K = \sum_{m=1}^{m_{\max}} \frac{f^{(i)}_m \eta^{(m)}_K}{\sqrt{n_m}}. \tag{9}$$

We can now define two types of the K-mixing. In *kinematic K-mixing* we have the situation where only one collective state is used (i.e., $m_{\max} = 1$). Then, the solution of the HW equation amounts to calculating only one matrix element of the Hamiltonian kernel,

$$E_1 = \bar{g}^{(1)\dagger}\mathcal{H}\bar{g}^{(1)} = \frac{\bar{\eta}^{(1)\dagger}\mathcal{H}\bar{\eta}^{(1)}}{n_1} \tag{10}$$

(i.e., $f^{(1)}_1 = 1$ and $f^{(1)}_m = 0$ for $m > 1$). In kinematic K-mixing, the mixing coefficients $g^{(1)}_K = \eta^{(1)}_K/\sqrt{n_1}$ are entirely determined by the norm kernel and do not depend on the Hamiltonian kernel (i.e., they are entirely given by the cranking approximation and Coriolis coupling). In contrast, with *dynamic K-mixing* we have the full solution of the HW equation for $m_{\max} > 1$, where the cutoff parameter ζ is adjusted to obtain a plateau condition for the lowest eigenvalue E_1. Here, the generator-coordinate-method (GCM) mixing of different K components becomes effective, which potentially can modify the cranking mixing coefficients. We stress here that kinematic K-mixing does correspond to a K-mixed

solution too and is not assuming any single given value of K.

The deformed CHF states were provided by the code HFODD, which solves the Hartree-Fock equations that correspond to the Ritz variational principle,

$$\delta \frac{\langle \Phi_{I_y} | \hat{H} - \omega \hat{I}_y | \Phi_{I_y} \rangle}{\langle \Phi_{I_y} | \Phi_{I_y} \rangle} = 0, \quad (11)$$

with angular frequency ω adjusted so as to fulfill constraint (1) and the value of I_y being equal to I, according to our $I_y \rightarrow I$ scheme. The y signature and parity symmetries were conserved. The Hamiltonian and overlap kernels were calculated by using the Gauss-Chebyshev quadrature in the α and γ directions and the Gauss-Legendre quadrature in the β direction [22]. In the numerical applications presented in this work we used the SLy4 [23] Skyrme force, but similar results were also obtained by using the SIII [24] force. The time-odd terms in the Skyrme functional were fixed by using values of the Landau parameters [25,26]. The harmonic-oscillator basis was composed of 10 spherical shells. The integration over the Euler angles was done by using a cube of $50 \times 50 \times 50$ integration points.

III. RESULTS

In Ref. [14], we demonstrated that, in a well-deformed nucleus ^{156}Gd, the AMP $I_y \rightarrow I$ scheme reproduces well the cranking MoI along the rotational band, after taking into account dynamic K-mixing. Here, we study the AMP methods applied to the terminating bands in the $A \sim 44$ region of nuclei.

A. Ground-state rotational band in ^{46}Ti

As a first example, consider the ground-state rotational band in ^{46}Ti. According to the CHF model, the shape of this nucleus undergoes a gradual change along the band. Starting from a well-elongated ($\beta_2 \sim 0.23$) shape at low spins, the nucleus goes through the alignment processes of the $f_{7/2}$ protons and neutrons, and eventually reaches a nearly spherical ($\beta_2 \sim 0.05$) shape at the terminating spin of $I = 14$, as shown in Fig. 1(a). The calculated and experimental ^{46}Ti rotational bands are shown in Fig. 1(b). Results of the CHF calculations (left) are compared to those of AMP (middle) and to experimental data (right). To visualize the role of K-mixing, we have depicted results of the AMP calculations separately for kinematic and dynamic K-mixing. For dynamic K-mixing, the AMP excitation energies were calculated from the plateau condition. The stability of results with respect to the number of natural states, m_{max}, is shown in Fig. 1(c). It can be seen that already at $m_{max} = 2$, a perfect stability is obtained (i.e., here, the difference between kinematic and dynamic K-mixing is related to adding the $m = 2$ state to the collective subspace). At higher values of m_{max}, one observes small departures from the converged values, which are due to accidental mixing with spurious solutions (with the largest such effect seen for $I = 4$ at $m_{max} = 5$). Nevertheless, physical converged solutions are clearly seen well beyond the point where the spurious solutions become lower in energy, as is well known for other GCM calculations [28].
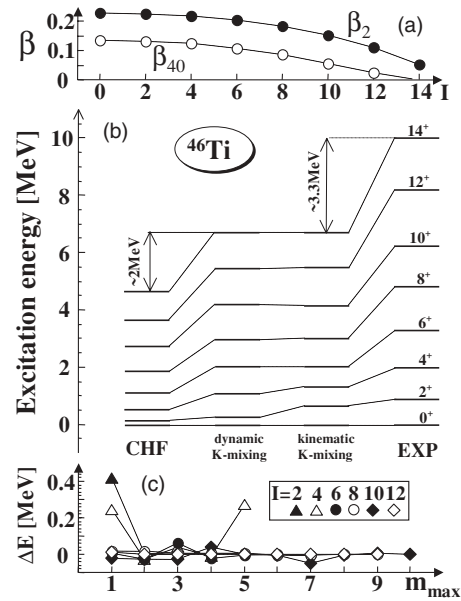

FIG. 1. Results of the CHF and AMP calculations for the rotational band in ^{46}Ti obtained for the SLy4 interaction. (a) The evolution of quadrupole and hexadecapole shape parameters along the band as calculated using the CHF approximation. (b) The excitation spectra calculated using the CHF approximation (left column) and AMP method with kinematic and dynamic K-mixing (middle columns), compared with the empirical data [27] (right column). (c) Deviations ΔE of energy levels with spins $I = 2, \dots, 12$ from the converged values corresponding to the plateau condition, as functions of the number m_{max} of the norm eigenvalues used when solving the HW equation.

Figure 1(b) clearly shows that, within the $I_y \rightarrow I$ scheme, the AMP effectively causes a decrease of the mean MoI within the band. This effect is expected to be generic for rotational bands of decreasing collectivity. Indeed, in such cases rotational correction is large at low spins and decreases at higher spins. This is illustrated in Fig. 2, where the calculated bands are shown in the absolute energy scale. In the case of ^{46}Ti, a net increase in the excitation energy of the terminating state, because of the AMP, amounts to about 2 MeV, but it is almost entirely related to the lowering of the $I = 0$ state, whereas the terminating $I = 14$ state remains almost unaffected by the AMP.

In the same figure, we also show for comparison the AMP spectrum obtained by projecting from the $\langle \hat{I}_y \rangle = 0$ ground state. In this case, the overall MoI turns out to be much too small and the excitation energy much too high as compared to the CHF or AMP $I_y \rightarrow I$ results. This fact once again shows the importance of the structural changes that occur in the system with increasing angular momentum.

Note that the $\langle \hat{I}_y \rangle = 0$ state is axial, and thus for all spins it contains only the $K = 0$ component. Therefore, here, the collective space contains only one state and there is no K-mixing at all. Moreover, axial symmetry leads to a tremendous simplification of the AMP method, whereby only one-dimensional integration over the Euler β angle is needed. Note also that the CHF states for $\langle \hat{I}_y \rangle \neq 0$ are never axial, because the Coriolis coupling always induces some nonzero
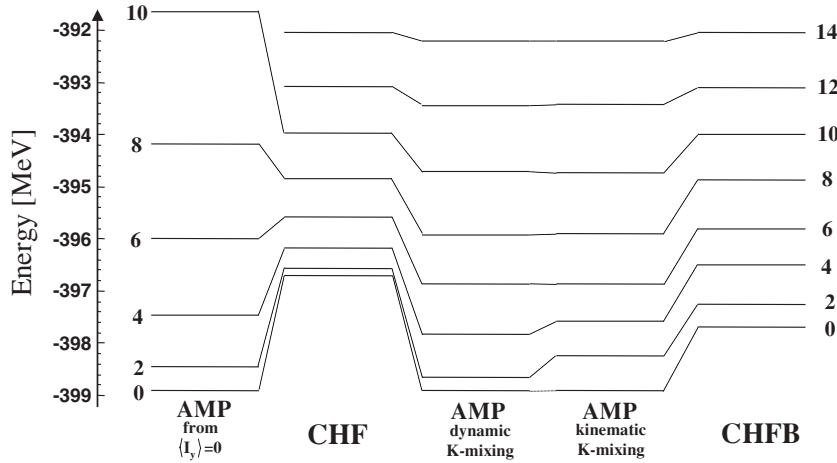
FIG. 2. Similar to Fig. 1(b), but shown in the absolute energy scale. Results of the AMP from the $\langle \hat{I}_y \rangle = 0$ ground state (first column) are compared to those of the CHF (second column), AMP with kinematic and dynamic K-mixing (third and fourth columns), and CHFB calculations (fifth column).

nonaxiality. Therefore, the full three-dimensional integration over the Euler angles $\alpha\beta\gamma$ is needed in our $I_y \rightarrow I$ scheme.

In the right column of Fig. 2, we also show results of the cranked Hartree-Fock-Bogolyubov calculations (CHFB) performed by using a zero-range volume-type (density-independent) interaction in the pairing channel. Its strengths of $V_n = -217.0$ and $V_p = -237.5$ MeV fm^{-3} for neutrons and protons, respectively, with a cutoff energy of $\epsilon_{cut} = 50$ MeV [29], were adjusted to reproduce, on average, the pairing gaps in this region of nuclei. For the $\langle \hat{I}_y \rangle = 0$ ground state of ^{46}Ti, the calculated gaps read $\Delta_n = 1.394$ and $\Delta_p = 1.632$ MeV.

One can see that, in comparison with the CHF results, pairing correlations only affect states at low spins, $I \leqslant 6$, and give about 1 MeV of additional binding at $\langle \hat{I}_y \rangle = 0$. Pairing correlations vanish in the terminating state, and thus its energy is the same within the CHF and CHFB methods. At present, the code HFODD cannot perform the AMP of paired states, and we are yet unable to evaluate the combined effects of pairing and AMP from cranked states.

It is also interesting to observe that, in the case of ^{46}Ti, the dynamic K-mixing is effective essentially only for $I = 2$ and 4 [see Figs. 1(b) and 1(c)]. This result is rather surprising, particularly in view of the fact that the only discontinuity in spatial anisotropy of the CHF solutions can be seen around spins $I \sim 6, 8$. This behavior is also qualitatively different from that found in ^{156}Gd [14], where dynamic K-mixing was effective up to the highest ($I \sim 20$) calculated spins. Apparently, the magnitude of K-mixing cannot be inferred solely from the shape but it also depends on individual (alignment) degrees of freedom.

In Fig. 3, we show probabilities W_I of finding the angular momentum components in the intrinsic CHF states, that is,

$$W_I = \sum_{K=-I}^{I} \langle \Phi_{I_y} | \hat{P}_{KK}^I | \Phi_{I_y} \rangle. \tag{12}$$

The inset also shows probabilities W_K of finding the given K components,

$$W_K = \langle \Phi_{I_y} | \hat{P}_{KK}^I | \Phi_{I_y} \rangle / W_I, \tag{13}$$

in one of the intrinsic states, $\langle \hat{I}_y \rangle = 6$. At low spins, the W_I probability distributions follow the general pattern of deformed collective states. This pattern suddenly disappears at the termination point of $\langle \hat{I}_y \rangle = 14$, where the CHF state becomes totally aligned, and therefore it contains only the single $I = 14$ component. The W_K probabilities do not follow the standard pattern of collective rotation, where they correspond to the Coriolis mixing only (cf. Fig. 2 in Ref. [14]).
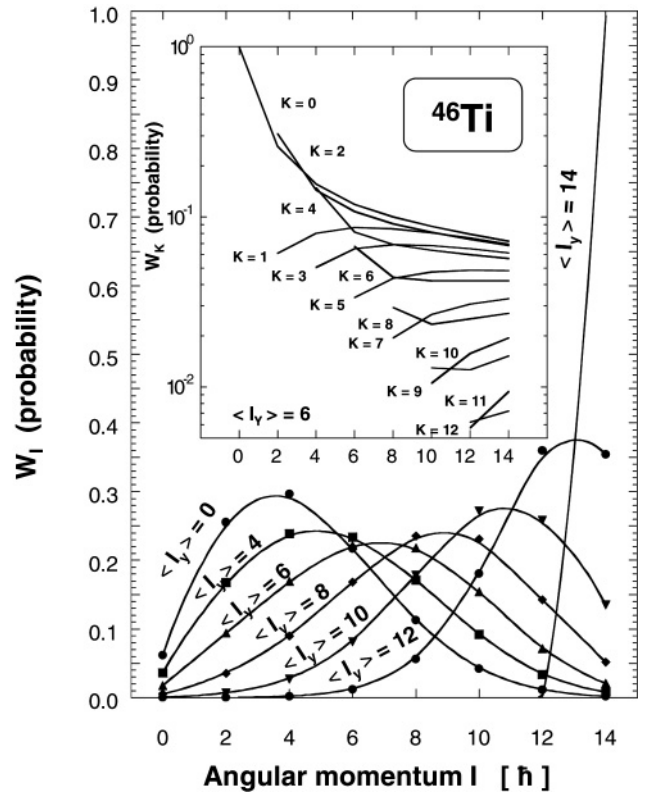

FIG. 3. Probabilities W_I (12) and W_K (13) of finding the given I and K components, respectively, in the intrinsic CHF states for different values of the projection on the y axis $\langle \hat{I}_y \rangle$. Solid lines are drawn only to guide the eye. Note that because of the conserved y-signature symmetry, one has $W_I = 0$ for odd values of I and $W_{-K} = W_K$.
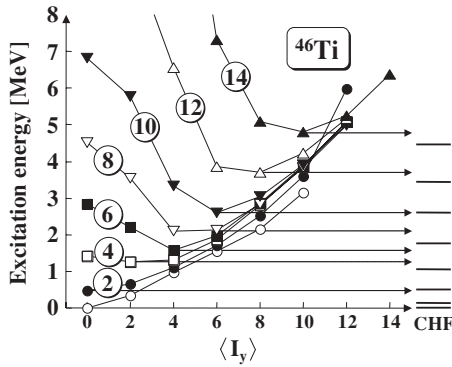
FIG. 4. Excitation spectra calculated using the AMP of CHF states constrained to different values of $\langle \hat{I}_y \rangle$, with kinematic K-mixing. Solid lines connect states of given projected angular momenta I and are drawn only to guide the eye. Arrows indicate the minimum energies as a function of $\langle \hat{I}_y \rangle$. For comparison, the right column shows the CHF spectrum.

Here, the aligning state causes the values of W_K to decrease with I and induces the crossing of those corresponding to even and odd K values as a function of I. Note also that the angular momentum aligns along the y axis, whereas the standard projections K are calculated with respect to the z axis. Therefore, we do not expect to see a single K component of the aligned $\langle \hat{I}_y \rangle = 14$ state.

We conclude this section by analyzing excitation spectra calculated by using the AMP of CHF states constrained to different values of $\langle \hat{I}_y \rangle$, as shown in Fig. 4. It turns out that the AMP energies minimized with respect to $\langle \hat{I}_y \rangle$, or equivalently with respect to the angular frequency ω, significantly differ from those obtained within our $I_y \rightarrow I$ scheme. Indeed, although the minimum $I = 0$ energy is obtained by projecting the $\langle \hat{I}_y \rangle = 0$ CHF state, this is not the case for $I > 0$ states. For example, the minimum $I = 2$ and 14 energies are obtained by projecting the $\langle \hat{I}_y \rangle = 0$ and 10 CHF states, respectively. The resulting excitation spectrum (in Fig. 4 indicated by arrows) is quite irregular and can hardly be associated with the physical result. This is because the minimization over ω does not constitute the full variation-after-projection minimization of energy, which should be performed in the complete parameter space, including, for example, the deformation parameters. Moreover, the fact that the $I = 14$ state may gain energy by using collective correlations on top of the fully aligned (terminating) state points out a possible inadequacy of the EDF method when it is used within the variation-after-projection procedure, and not within the $I_y \rightarrow I$ projection-after-variation scheme.

B. Angular momentum projection near the band termination

In the vicinity of band termination, the number of contributing configurations drops and the physics simplifies significantly. Reliable approximate analytical symmetry restoration schemes can be easily derived for these cases; for details we refer the reader to the analysis presented recently in Refs. [30,31]. In the present paper we aim at further study and testing of these approximate methods against rigorous AMP results.

Let us first consider the energy splittings between the favored- and unfavored-signature terminating states, $[f_{7/2}^n]_{I_{\max}}$ and $[f_{7/2}^n]_{I_{\max}-1}$, respectively, within the $[f_{7/2}^n]$ configurations, where n denotes the number of particles in the $f_{7/2}$ subshell. Within the naive noncollective cranking model, the unique aligned $|\Phi_{I_{\max}}\rangle$ states can be considered as many-body reference states (HF vacua) with projections of the angular momentum being conserved quantum numbers equal to the maximum allowed values, $I_y = I_{\max}$. From these local HF vacua, the $|\Phi_{I_{\max}-1}^{(\tau)}\rangle$ states can be generated by particle-hole (ph) excitations, in particular, by changing the signature of either a single neutron ($\tau = \nu$) or a single proton ($\tau = \pi$). In spite of the fact that the underlying CHF solutions are almost spherical, they manifestly break the rotational invariance. Indeed, the two $I_{\max} - 1$ CHF solutions have conserved projections of the angular momentum, $I_y = I_{\max} - 1$, but are in this case linear combinations of the total angular momentum states with $I = I_{\max}$ and $I_{\max} - 1$, that is, up to a normalization factor:

$$
\begin{aligned}
\left|\Phi_{I_{\max}-1}^{(\pi)}\right\rangle &\sim b|I_{\max}; I_{\max} - 1\rangle + a|I_{\max} - 1; I_{\max} - 1\rangle, \\
\left|\Phi_{I_{\max}-1}^{(\nu)}\right\rangle &\sim a|I_{\max}; I_{\max} - 1\rangle - b|I_{\max} - 1; I_{\max} - 1\rangle.
\end{aligned}
\tag{14}
$$

The simplicity of the encountered situation allows for an approximate analytical estimate of mixing coefficients a and b [30,31]. Equivalently, one can find these coefficients by performing the exact AMP of the $|\Phi_{I_{\max}-1}^{(\pi)}\rangle$ or $|\Phi_{I_{\max}-1}^{(\pi)}\rangle$ states. The resulting probabilities $P(I_{\max} - 1)$ of finding the $I_{\max} - 1$ components within the $|\Phi_{I_{\max}-1}^{(\pi)}\rangle$ states are shown in Fig. 5(a). The AMP results match perfectly the analytical results obtained in Refs. [30,31], confirming the reliability of the approximate method.

Calculated energy differences $E(I_{\max}) - E(I_{\max} - 1)$ are shown in Fig. 5(b). Because the CHF solutions break the isobaric invariance, the AMPs of the $|\Phi_{I_{\max}-1}^{(\pi)}\rangle$ and $|\Phi_{I_{\max}-1}^{(\nu)}\rangle$ states are not fully equivalent and lead to slightly different energies. Results shown in Fig. 5 represent arithmetic averages of both AMP energies. The only exception is ^{42}Sc, where we were able to perform numerical integration with a desired accuracy only when projecting from the $|\Phi_{I_{\max}-1}^{(\nu)}\rangle$ CHF state, and the depicted point represents this single result. It is evident from the figure that, except for ^{42}Sc and ^{45}Sc, the quality of the results is comparable to the state-of-the-art shell-model calculations of Refs. [31,32].

The unfavored-signature $I_{\max} - 1$ CHF states just discussed were created by building the signature-inverting ph excitations on top of the $I_{\max}$ reference state. A similar procedure applied to create $I_{\max} - 2$ CHF solutions leads to several nearly spherical states, located, on average, above the reference state.

In this case, however, the SSB mechanism enters the game by pushing the collective (deformed) CHF solution down, below the reference state, and relatively close to the empirical energy. Hence, by going from the $I_{\max} - 1$ to $I_{\max} - 2$ states, the physics changes quite dramatically, showing clearly two contrasting facets of the SSB mechanism of rotational symmetry in nuclear physics.

In the case of the $I_{\max} - 1$ states, the symmetry restoration results in a repulsion of two nearly degenerate proton and
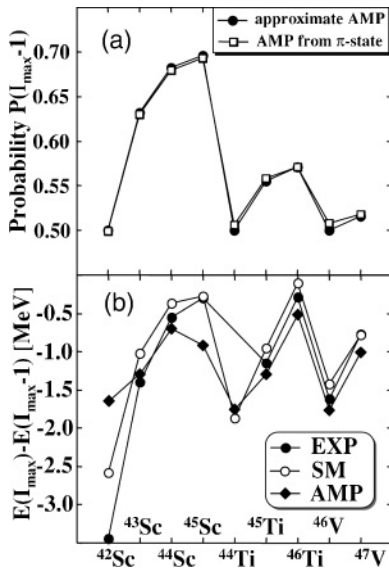
FIG. 5. (a) Probabilities of finding the $I_{max} - 1$ spin components in the $|\Phi_{I_{max}-1}^{(\pi)}\rangle$ CHF solutions. Squares and dots show results calculated using the exact AMP and approximate method of Ref. [30], respectively. (b) Energy differences between the favored- and unfavored-signature terminating states, $[f_{7/2}^n]_{I_{max}}$ and $[f_{7/2}^n]_{I_{max}-1}$, respectively. Values calculated using the AMP method (diamonds) are compared to those obtained within the shell model [30] (circles) and empirical data [33–38] (dots).

neutron CHF states, which are located above the reference I_{max} state. On the one hand, the reorientation mode, $|I_{max}; I_{max} - 1\rangle$, is shifted downward and becomes degenerate with the $|I_{max}; I_{max}\rangle$ solution, as required by the rotational invariance. On the other hand, the physical mode, $|I_{max} - 1; I_{max} - 1\rangle$, is shifted upward and becomes the unfavored-signature terminating state.

In the case of the $I_{max} - 2$ states, the SSB mechanism results in a repulsion of several nearly degenerate proton and neutron ph states. The collective CHF mode, $|\Phi_{I_{max}-2}\rangle$, is shifted below the reference I_{max} state, in accordance with data. By the AMP mixing, the symmetry-restored collective mode projected from $|\Phi_{I_{max}-2}\rangle$ (i.e., the $|I_{max} - 2; I_{max} - 2\rangle$ state) gains some additional binding energy. This situation is schematically illustrated in the inset of Fig. 6.

The calculated energy differences, $E(I_{max}) - E(I_{max} - 2)$, are shown in Fig. 6. The CHF solutions, except for ^{42}Ca and ^{42,43}Sc, correspond to collective states having $\beta_2 \sim 0.10$–0.12. The AMP shifts these states almost uniformly down by about 300–400 keV, enlarging the splitting by that amount and improving an overall agreement between theory and experiment. It is, however, evident from the figure that, here, the AMP does not improve upon the incorrect isotopic/isotonic dependence of the CHF results. The magnitude of rotational correction is determined predominantly by the shape change and does not vary from case to case. One can speculate that a detailed agreement with data would require an additional isospin-symmetry restoration.

A similar trend was found for the $I_{max} - 2$ states for configurations involving one-proton ph excitation from the $d_{3/2}$ to $f_{7/2}$ subshell (see Fig. 7). Here, all the lowest $I_{max} - 2$
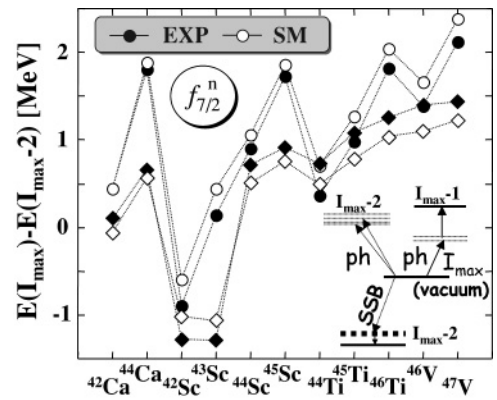

FIG. 6. Energy differences between the $[f_{7/2}^n]_{I_{max}}$ terminating states and the lowest $[f_{7/2}^n]_{I_{max}-2}$ states. Filled and unfilled circles represent the empirical data [33–39] and SM results of Ref. [30], respectively. Unfilled diamonds label the lowest CHF solutions, which are collective except for the cases of ^{42}Ca and ^{42,43}Sc. Filled diamonds represent the AMP results. Relative energies among the I_{max} reference state, noncollective ph $I_{max} - 1$ and $I_{max} - 2$ excitations (thin lines), SSB effect in the $I_{max} - 2$ state (thick dashed line), and final AMP configuration mixing (solid lines) are schematically illustrated in the inset.

states are found to be deformed. The energy gain from the AMP is again of the order of 300–400 keV and weakly depends on N and Z, thus merely reflecting an increase of deformation between nearly spherical I_{max} states and terminating collective cranking solutions for $I_{max} - 2$. This example confirms that the onset of collectivity causes a uniform mixing of various angular momenta, regardless of individual features of specific nuclei. Indeed, in the studied nuclei, the probabilities of finding the $I_{max} - 2$ spin component within the $|\Phi_{I_{max}-2}\rangle = \sum_I w_I |I\rangle$ CHF deformed wave packets are $|w_{I_{max}-2}|^2 = 0.34 \pm 0.05$ (i.e., they depend extremely weakly on N and Z). Moreover, values of $|w_{I_{max}-2}|^2$ appear to be very similar to $|w_{I_{max}}|^2$, which are equal to 0.35 ± 0.04, and again these almost do not change from one nucleus to another.
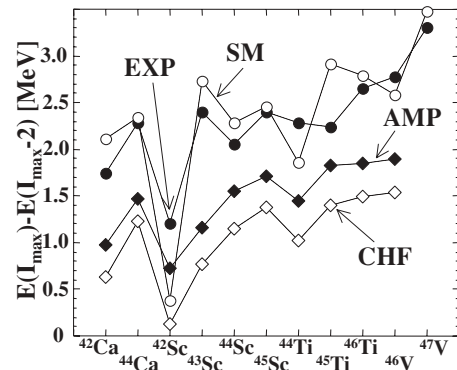

FIG. 7. Energy differences between the $[d_{3/2}^{-1} f_{7/2}^{n+1}]_{I_{max}}$ terminating states and the lowest $[d_{3/2}^{-1} f_{7/2}^{n+1}]_{I_{max}-2}$ states. Filled and unfilled circles represent empirical data [33–39] and SM results of Ref. [30], respectively. Filled and unfilled diamonds label the AMP results and the collective CHF solutions, respectively.
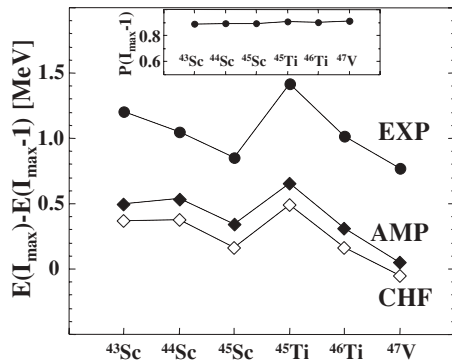
FIG. 8. Energy differences between the $[d_{3/2}^{-1} f_{7/2}^{n+1}]_{I_{max}}$ terminating states and the lowest unfavored-signature terminating $d_{3/2}^{-1} f_{7/2}^{n+1}]_{I_{max}-1}$ states. Filled circles represent empirical data [34–39] and unfilled and filled diamonds represent the CHF and AMP results, respectively. The inset shows the probabilities of finding the $I_{max} - 1$ components within the lowest CHF solution $|\Phi_{I_{max}-1}\rangle$.

The situation changes quite radically for the unfavored-signature $[d_{3/2}^{-1} f_{7/2}^{n+1}]_{I_{max}-1}$ states. Within the CHF approximation, in $N \neq Z$ and $N \neq Z + 1$ nuclei there are three $I_{max} - 1$ configurations that can be created from the I_{max} reference state. Indeed, this can be done by a signature-inverting ph excitation involving either the neutron (ν) or proton (π) $f_{7/2}$ particle, or the proton $d_{3/2}$ hole ($\bar{\pi}$) (see Ref. [30]). The CHF solutions represent, therefore, mixtures of two physical $|I_{max} - 1; I_{max} - 1\rangle_i$, $i = 1, 2$, states with the spurious reorientation $|I_{max}; I_{max} - 1\rangle$ mode.

In such a case, the $I_y \to I$ AMP scheme only removes the spurious mode, not affecting the mixing ratio of the two physical solutions $|I_{max} - 1; I_{max} - 1\rangle_i$, $i = 1, 2$. Hence, in contrast with the case of the $[f_{7/2}^n]_{I_{max}-1}$ states, the quality of the results strongly depends on the quality of the underlying CHF field. The AMP results corresponding to the $\bar{\pi}$ CHF solutions, which in $^{42-45}$Sc, $^{44-46}$Ti, and ^{47}V are the lowest in energy, show that the admixtures of spurious components are of the order of 10% (see the inset in Fig. 8). The obtained rotational corrections are, therefore, small—of the order of 100–20 keV, and the disagreement with data remains quite large, as shown in Fig. 8. We show these results only as an example of possible AMP calculations. However, for a complete analysis, one should, in principle, perform the GCM mixing of the AMP states corresponding to any possible CHF $I_{max} - 1$ configuration. A study in this direction is left for future work.

IV. SUMMARY AND DISCUSSION

The present work reports on the first systematic calculations using the AMP of cranked Hartree-Fock states. The technique used, called the $I_y \to I$ projection scheme, assumes the projection of the angular momentum component I from the one-dimensional (1D) cranked Hartree-Fock solution constrained to $\langle \hat{I}_y \rangle = I$. The method benefits naturally from such nice physical features of the 1D cranking model as the shape-spin self-consistency or the ability to get a realistic

estimate of the nuclear MoI. It is shown that the $I_y \to I$ AMP scheme leads to values of MoI that are much more realistic than those obtained by using the AMP of nonrotating $\langle \hat{I}_y \rangle = 0$ states, as was the common practice up to now.

In particular, application of the scheme to the rotational band in ^{46}Ti clearly improves the MoI at the bottom of the band. It also reveals a simple mechanism by which rotational corrections allow for improving upon an incorrect excitation energy of the terminating state, $\Delta E_{I_{max}}$, obtained in the CHF calculations, which account only for roughly half of the empirical value.

Pairing correlations that are active in the ground state, but do not affect the fully aligned terminating state, can heal the situation only partially. Indeed, there is an upper limit for pairing correlation energy in the ground state, which can be sustained by a deformed $A \sim 44$ system, equal to about 2 MeV. Further enhancement of pairing would induce the phase transition from deformed to spherical shape [40], and the rotational band could not have been built, contradicting the experimental data. Together, the rotational and pairing effects can bring $\Delta E_{I_{max}}$ to about 9 MeV (i.e., some $\sim 10\%$ below the experimental value). Let us mention here that for the $I = 14$ state projected from the $\langle \hat{I}_y \rangle = 0$ ground state one obtains $\Delta E_{I_{max}} \simeq 19$ MeV (i.e., a result that is well above the empirical excitation energy of the terminating state).

For nearly spherical unfavored-signature $[f_{7/2}^n]_{I_{max}-1}$ terminating states, our AMP calculations give results in excellent agreement with data, and they validate the approximate projection methods introduced in Refs. [30,31]. We also show that the onset of collectivity in the $[f_{7/2}^n]_{I_{max}-2}$ states is quite correctly reproduced by the CHF calculations, on top of which the AMP gives only a small correction going in the right direction in comparison with data. However, details of the isotopic dependence are not reproduced here.

Similar conclusions are obtained for the $[d_{3/2}^{-1} f_{7/2}^{n+1}]$ configurations that involve one-proton ph excitation across the $Z = 20$ shell gap. In this case, in both $I_{max} - 1$ and $I_{max} - 2$ states near the band termination the collectivity sets in, whereas the energy differences with respect to terminating I_{max} states are underestimated in the CHF and AMP calculations.

The AMP of cranked Hartree-Fock states presented in this work was performed by applying the standard projection techniques to the CHF solutions obtained within the EDF method. We have checked that all the results are stable with respect to numerical parameters such as, for example, numbers of integration points used when integrating kernels over the Euler angles. Nonetheless, one should be aware of potential risks caused by difficult-to-control, uncompensated poles plaguing projection techniques of states obtained within the EDF method [14,41]. Clearly, the future of projection methods crucially depends on a satisfactory solution of the problem of such singularities.

[1] P. Hohenberg and W. Kohn, Phys. Rev. **136**, B864 (1964); W. Kohn and L. J. Sham, *ibid.* **140**, A1133 (1965); W. Kohn, Rev. Mod. Phys. **71**, 1253 (1998).

[2] A. V. Afanasjev, D. B. Fossan, G. J. Lane, and I. Ragnarsson, Phys. Rep. **322**, 1 (1999).

[3] K. W. Schmid, F. Grümmer, and A. Faessler, Phys. Rev. C **29**, 291 (1984).

[4] A. Valor, P.-H. Heenen, and P. Bonche, Nucl. Phys. **A671**, 145 (2000).

[5] R. Rodriguez-Guzmán, J. L. Egido, and L. M. Robledo, Nucl. Phys. **A709**, 201 (2002).

[6] K. W. Schmid, F. Grümmer, and A. Faessler, Ann. Phys. (NY) **180**, 1 (1987).

[7] K. Hara and Y. Sun, Int. J. Mod. Phys. E **4**, 637 (1995).

[8] M. Bender, P.-H. Heenen, and P.-G. Reinhard, Rev. Mod. Phys. **75**, 121 (2003).

[9] W. Satuła and R. Wyss, Rep. Prog. Phys. **68**, 131 (2005).

[10] R. A. Sorensen, Nucl. Phys. **A281**, 475 (1977).

[11] R. Bengtsson and H.-B. Håkansson, Z. Phys. A **288**, 193 (1978).

[12] S. Islam, H. J. Mang, and P. Ring, Nucl. Phys. **A326**, 161 (1979).

[13] D. Baye and P.-H. Heenen, Phys. Rev. C **29**, 1056 (1984).

[14] H. Zduńczuk, J. Dobaczewski, and W. Satuła, Int. J. Mod. Phys. E **16**, 377 (2007).

[15] J. Dobaczewski *et al.*, Comput. Phys. Commun. **131**, 164 (2000); **158**, 158 (2004); HFODD User's Guide, nucl-th/0501008 (see also http://www.fuw.edu.pl/dobaczew/hfodd/hfodd.html).

[16] J. Dobaczewski, W. Satuła, J. Engel, P. Olbratowski, P. Powałowski, M. Sadziak, A. Staszczak, M. Zalewski, and H. Zduńczuk, Comput. Phys. Commun. (to be published).

[17] R. E. Peierls and J. Yoccoz, Proc. Phys. Soc. (London) **A70**, 381 (1957).

[18] P. Ring and P. Schuck, *The Nuclear Many Body Problem* (Springer-Verlag, Berlin, 1980).

[19] D. A. Varshalovich, A. N. Moskalev, and V. K. Kersonskii, *Quantum Theory of Angular Momentum* (World Scientific, Singapore, 1988).

[20] D. L. Hill and J. A. Wheeler, Phys. Rev. **89**, 1102 (1953).

[21] L. M. Robledo, Int. J. Mod. Phys. E **16**, 337 (2007).

[22] M. Abramowitz and I. A. Stegun, *Handbook of Mathematical Functions* (Dover, New York, 1970).

[23] E. Chabanat, P. Bonche, P. Haensel, J. Meyer, and F. Schaeffer, Nucl. Phys. **A635**, 231 (1998).

[24] M. Beiner, H. Flocard, N. Van Giai, and P. Quentin, Nucl. Phys. **A238**, 29 (1975).

[25] M. Bender, J. Dobaczewski, J. Engel, and W. Nazarewicz, Phys. Rev. C **65**, 054322 (2002).

[26] H. Zduńczuk, W. Satuła, and R. A. Wyss, Phys. Rev. C **71**, 024305 (2005).

[27] F. Brandolini, J. R. B. Oliveira, N. H. Medina, R V. Ribas, J. Sanchez-Solano, D. Bucurescu, S. M. Lenzi, C. A. Ur, D. Bazzacco, M. De Poli, E. Farnea, A. Gadea, N. Marginean, and C. Rossi-Alvarez, Phys. Rev. C **70**, 034302 (2004).

[28] P. Bonche, J. Dobaczewski, H. Flocard, P.-H. Heenen, and J. Meyer, Nucl. Phys. **A510**, 466 (1990).

[29] P. J. Borycki, J. Dobaczewski, W. Nazarewicz, and M. V. Stoitsov, Phys. Rev. C **73**, 044319 (2006).

[30] M. Zalewski and W. Satuła, Int. J. Mod. Phys. E **16**, 386 (2007).

[31] M. Zalewski, W. Satuła, W. Nazarewicz, G. Stoitcheva, and H. Zduńczuk, Phys. Rev. C **75**, 054306 (2007).

[32] G. Stoitcheva, W. Satuła, W. Nazarewicz, D. J. Dean, M. Zalewski, and H. Zduńczuk, Phys. Rev. C **73**, 061304(R) (2006).

[33] S. M. Lenzi, D. R. Napoli, C. A. Ur, D. Bazzacco, F. Brandolini, J. A. Cameron, E. Caurier, G. de Angelis, M. De Poli, E. Farnea, A. Gadea, S. Hankonen, S. Lunardi, G. Martínez-Pinedo, Zs. Podolyak, A. Poves, C. Rossi Alvarez, J. Sánchez-Solano, and H. Somacal, Phys. Rev. C **60**, 021303(R) (1999).

[34] P. Bednarczyk, W. Meczyński, J. Styczeń, J. Grebosz, M. Lach, A. Maj, M. Ziebliński, N. Kintz, J. C. Merdinger, N. Schulz, J. P. Vivien, A. Bracco, J. L. Pedroza, M. B. Smith, and K. M. Spohr, Acta Phys. Pol. B **32**, 747 (2001).

[35] F. Brandolini, N. H. Medina, D. Bazzacco, J. A. Cameron, G. de Angelis, A. Gadea, N. Menegazzo, and C. Rossi-Alvarez, Nucl. Phys. **A693**, 517 (2001).

[36] M. Lach, J. Styczeń, W. Meczyński, P. Bednarczyk, A. Bracco, J. Grebosz, A. Maj, J. C. Merdinger, N. Schultz, M. B. Smith, K. M. Spohr, and M. Ziebiński, Eur. Phys. J. A **25**, 1 (2005).

[37] C. J. Chiara, M. Devlin, E. Ideguchi, D. R. LaFosse, F. Lerma, W. Reviol, S. K. Ryu, D. G. Sarantites, O. L. Pechenaya, C. Baktash, A. Galindo-Uribarri, M. P. Carpenter, R. V. F. Janssens, T. Lauritsen, C. J. Lister, P. Reiter, D. Seweryniak, P. Fallon, A. Gorgen, A. O. Macchiavelli, D. Rudolph, G. Stoitcheva, and W. E. Ormand, Phys. Rev. C **75**, 054305 (2007); **75**, 059904(E) (2007).

[38] S. Lenzi and J. Styczeń (private communication).

[39] M. Lach, J. Styczeń, W. Meczyński, P. Bednarczyk, A. Bracco, J. Grebosz, A. Maj, J. C. Merdinger, N. Schultz, M. B. Smith, K. M. Spohr, J. P. Vivien, and M. Ziebiński, Eur. Phys. J. A **16**, 309 (2003).

[40] W. Satuła, Int. J. Mod. Phys. E **16**, 360 (2007).

[41] J. Dobaczewski, M. V. Stoitsov, W. Nazarewicz, and P.-G. Reinhard, submitted to Phys. Rev. C, arXiv:0708.0441.